

# Tip-Enhanced Dark Exciton Nanoimaging and Local Strain Control in Monolayer WSe<sub>2</sub>

Kathryn Hasz, Zuocheng Hu, Kyoung-Duck Park,\* and Markus B. Raschke\*



Cite This: *Nano Lett.* 2023, 23, 198–204



Read Online

ACCESS |

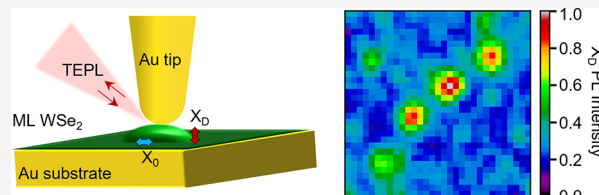
Metrics & More

Article Recommendations

Supporting Information

**ABSTRACT:** Dark excitons in transition-metal dichalcogenides, with their long lifetimes and strong binding energies, provide potential platforms from photonic and optoelectronic applications to quantum information science even at room temperature. However, their spatial heterogeneity and sensitivity to strain is not yet understood. Here, we combine tip-enhanced photoluminescence spectroscopy with atomic force induced strain control to nanoimage dark excitons in WSe<sub>2</sub> and their response to local strain. Dark exciton emission is facilitated by out-of-plane picocavity Purcell enhancement giving rise to spatially highly localized emission, providing for higher spatial resolution compared to bright exciton nanoimaging. Further, tip-antenna-induced dark exciton emission is enhanced in areas of higher strain associated with bubbles. In addition, active force control shows dark exciton emission to be more sensitive to strain with both compressive and tensile lattice deformation facilitating emission. This interplay between localized strain and Purcell effects provides novel pathways for nanomechanical exciton emission control.

**KEYWORDS:** tip-enhanced photoluminescence (TEPL), transition-metal dichalcogenides (TMDs), tungsten diselenide (WSe<sub>2</sub>), strain, nanobubbles



Transition-metal dichalcogenides (TMDs) are a class of 2D materials with a wide range of novel and unusual optical properties. When they are reduced to monolayer thickness, the transition from an indirect to a direct band gap gives rise to increased quantum confinement.<sup>1–5</sup> An associated strong exciton binding energy holds promise for optoelectronic and photonic applications.<sup>6–8</sup> For monolayer TMDs, strong spin-orbit coupling leads to a split of the conduction band with an optically dipole allowed bright exciton and forbidden dark exciton transition at the *K* and *K'* points in the Brillouin zone.<sup>2,9–14</sup> In WSe<sub>2</sub>, the dark exciton has an energy ~40 meV below that of the bright exciton. Due to its spin-forbidden transition, the radiatively dark exciton exhibits a much longer radiative lifetime, estimated to be as long as hundreds of nanoseconds,<sup>10,15,16</sup> than the dipole-allowed bright exciton emission.<sup>17</sup> Based on such long lifetimes, dark excitons were suggested for Bose-Einstein exciton condensation<sup>18</sup> or to serve as coherent two-level quantum systems.<sup>19</sup>

Further, the out-of-plane orientation of the dark exciton dipole moment makes its emission difficult to detect using conventional far-field spectroscopy in normal incidence with in-plane polarization. Spectroscopy of dark excitons at room temperature is further challenged by the thermally activated depopulation into the fast-emitting bright state. However, at low temperature by suppressing depopulation into the bright state,<sup>2</sup> combined with an applied magnetic field to partially tilt the spin,<sup>10,20</sup> or by coupling to surface plasmon polaritons,<sup>11,12</sup> their emission has been detected. More recently at room temperature, coupling dark excitons to plasmonic nano-

particles<sup>13</sup> statically, or more universally by forming a tunable picocavity in tip-enhanced photoluminescence (TEPL), allows for Purcell-enhanced spectroscopy and radiative control of dark excitons.<sup>14</sup>

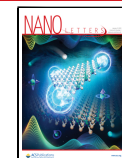
However, previous dark exciton spectroscopy has been limited to, at best, local point spectroscopy<sup>13,14</sup> or low-resolution micro-PL.<sup>10,11,20</sup> In addition, the effect of nanoscale spatial heterogeneities and the important role of strain on the dark excitonic behavior have remained unresolved. Chemical heterogeneities, defects, grain boundaries, edges, bubbles, etc. create trap states and modify exciton energies directly or indirectly through associated strain.<sup>12,21–28</sup> Strain induced through hydrostatic pressure, local nanoindentation, or bubbles has been shown to red shift the exciton emission as the crystal lattice deforms and reduces the band gap by 100 meV or more.<sup>21,22,26,28,29</sup>

Here, we use correlative TEPL and atomic force microscopy (AFM) force control for spectroscopic nanoimaging of bright and dark exciton emission and their response to strain in monolayer WSe<sub>2</sub>. In contrast to conventional near-field spectroscopy, which aims to be minimally invasive, we

Received: October 9, 2022

Revised: December 6, 2022

Published: December 20, 2022



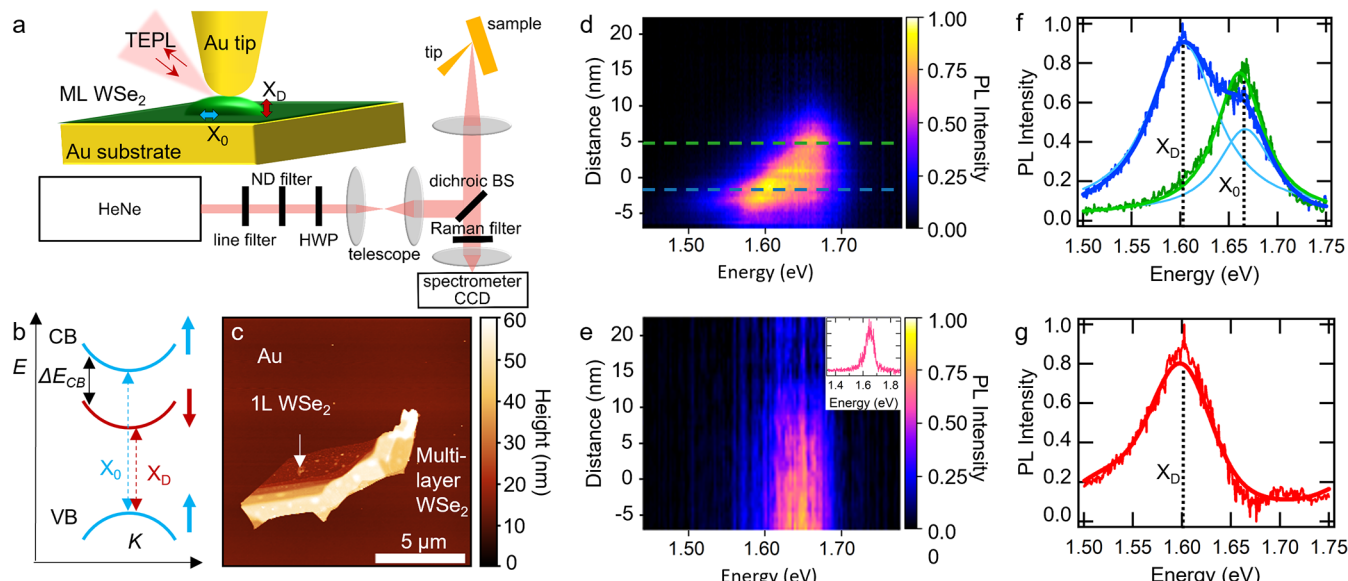


**Figure 1.** (a) Schematic of TEPL with cantilever gold tips for calibrated force control. (b) Band diagram of WSe<sub>2</sub> with bright X<sub>0</sub> and dark exciton X<sub>D</sub> states. (c) Topography of WSe<sub>2</sub> monolayer flake. (d) Spectral intensity vs cantilever-sample distance with laser polarization parallel with respect to the tip. (e) Corresponding TEPL distance scan with laser polarization perpendicular with respect to the tip with an example spectrum (inset). (f) Spectra from cross sections at different z positions at z = 4 nm (green) and z = -2 nm (blue) indicated by dotted lines. (g) Difference spectrum between them exhibiting distinct bright X<sub>0</sub> and dark exciton X<sub>D</sub> emission.

combine Purcell-enhanced picocavity coupling with active AFM force-induced local indentation. Due to their different lifetimes, a distinctly higher few-nanometer spatial confinement of the dark exciton emission is observed compared to bright excitons with longer-range near-field enhancement. In nano-imaging dark exciton emission from both planar regions and nanobubbles, we find that both tensile and compressive strain increase both bright and dark exciton emission compared to unstrained areas, correlated with a strain-induced spectral energy shift. Subsequent local force application in selected prestrained and unstrained regions then allows for dark exciton emission control over a wide parameter range at the interplay between picocavity Purcell enhancement, tip–sample-induced quenching, and nanomechanical local strain effects. The resulting systematic modification of bright and dark exciton emission can form the basis for developing active multi-excitonic photonic, optoelectronic, and optomechanical TMD devices.

For our experiment we employed a TEPL setup as shown in Figure 1a, based on an AFM (AIST, Horiba) using gold-coated cantilever tips (Omni-TERS SNC Au,  $f = 150$  kHz, Horiba), integrated into a home-built optical setup. Cantilever spring constants were calculated using the Sader method<sup>30</sup> and combined with measured cantilever deflection to quantitatively determine force values. Applied forces ranged from  $-60$  to  $+150$  nN, with most measurements performed in the range of  $-50$  to  $+70$  nN. The optical layout consisted of a continuous-wave 632.8 nm (1.96 eV) HeNe laser (HNL210L, Thorlabs), with the beam passing a half-wave plate for polarization control and a  $45^\circ$  dichroic beam splitter ( $T > 93\%$ , 641–980 nm, Thorlabs) focused on the tip–sample junction at a  $60^\circ$  angle of incidence with respect to the sample surface using an objective lens (NA = 0.28,  $f = 20$  mm, Mitutoyo). The epi-illumination/detection micro-PL and TEPL signal, reflected by the dichroic beam splitter, passed a long-pass filter with a cutoff of 641 nm (Thorlabs) and was then focused into the spectrometer ( $f =$

320 mm, 150 g/mm, iHR320, Horiba) and detected using a thermoelectrically cooled CCD camera (SynapseEM, Horiba).

WSe<sub>2</sub> monolayers were exfoliated from a bulk crystal (2D Semiconductors) using polydimethylsiloxane (PDMS) onto an  $\sim 100$  nm thick template-stripped Au film deposited on a Si substrate. Samples were precharacterized by AFM (Multimode, Bruker) and micro-PL to verify layer thickness (see Figure 1c).

As a general measurement protocol, sample topography and two spectra were measured at each image pixel while raster scanning the sample, with one spectrum in tip–sample force interaction for near-field signal acquisition ( $F = 5$  nN, defined as  $z = 0$  nm), referenced against a spectrum with the tip retracted ( $F = 0$  nN,  $z > 80$  nm), acquiring the far-field background (for details see the Supporting Information). Approach curves (spatirospectral z scans) were acquired with a user-specified cutoff force value. Approach curves were acquired with laser polarization both parallel and perpendicular with respect to the tip axis. This served to differentiate and act as a consistency check, with dark exciton emission only prominent with laser polarization parallel to the tip axis for enhanced out-of-plane optical field.

Figure 1d,e shows spatirospectral TEPL approach curves on a flat WSe<sub>2</sub> region after far-field background subtraction for tip parallel (Figure 1d) and tip perpendicular (Figure 1e) polarized excitation, respectively. As expected, and correlated with tip radius, few-nanometer localized TEPL emission is observed as the tip–sample distance decreases and the near-field signal emerges. Figure 1f shows two extracted representative spectra from Figure 1d at different tip–sample distances as indicated. For  $z = 10$  nm (green) only a single peak is observed, fitted with a single Lorentzian with a peak position of 1.655 eV characteristic of bright exciton X<sub>0</sub> emission. With decreasing distance the emergence of a second peak at lower energy, with a peak position of 1.60 eV as determined from a bi-Lorentzian fit (light blue line), signifies the emergence of the dark exciton X<sub>D</sub> emission. The 55 meV

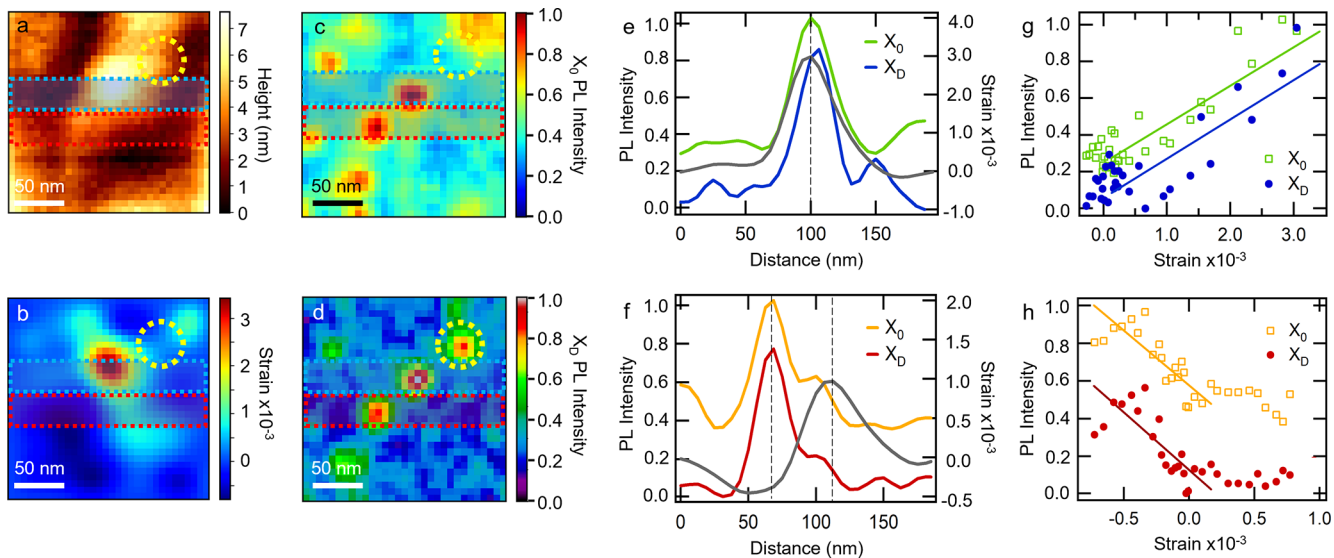


**Figure 2.** (a) Topography, (b) strain, (c) bright exciton intensity, and (d) dark exciton  $X_D$  intensity across a  $200 \times 200 \text{ nm}^2$  scan area of monolayer WSe<sub>2</sub>. Averaged cross sections of intensities and strain (e) for blue dotted regions in (c) and (d) and correspondingly (f) for red dotted regions. Corresponding increase in bright  $X_0$  and dark exciton  $X_D$  emission with both tensile (g) and compressive (h) strain for the data shown in (e) and (f), respectively.

energy difference is consistent with past results ranging from 30 to 60 meV for dark excitons in WSe<sub>2</sub>.<sup>2,10,13,14</sup>

As can be seen, the short distance for dark exciton emission with peak intensity at  $\sim 3$  nm already correlates with an onset of bright exciton quenching. This is a result of the considerable differences in radiative lifetimes between bright and dark excitons. Here, the small mode volumes in the picocavity necessary for efficient Purcell-enhanced dark exciton emission competes with the increase in nonradiative damping of the bright exciton due to dipole coupling and energy transfer with Drude relaxation in the metal substrate and tip. Figure 1g then shows the bright exciton normalized difference spectrum, exhibiting the isolated dark exciton response. For comparison, for tip perpendicular polarization, only weak bright exciton emission is observed with the distance dependence being shown in Figure 1e.

Figure 2a shows the AFM topography of a  $200 \times 200 \text{ nm}^2$  sample area of the WSe<sub>2</sub> monolayer selected for a representative distribution of bubbles of few-nanometer height. Figure 2b shows the corresponding strain map calculated from the topography following the method of Darlington et al.<sup>31</sup> based on the gradient of the surface topography and associated local curvature of bending of the WSe<sub>2</sub> monolayer. The method is derived from classical elastic plate theory through the Föppl–von Kármán equations.<sup>32–34</sup>

We then performed full spatiotemporal imaging and analyzed bright and dark exciton emission from spectral fitting at each image pixel as illustrated above. Figure 2c,d show the extracted intensity maps for bright (Figure 2c) and dark (Figure 2d) exciton emission. Data were taken at a set point of  $F = +5 \text{ nN}$  ( $z = 0 \text{ nm}$ ). The near-field signal was isolated by subtracting the far-field background. Image data were smoothed with a three-point filter to reduce the scatter induced by fitting errors. Despite only small topographic variations a spatially more varied heterogeneity was observed in both bright and dark exciton emission on length scales as short as a few tens of nanometers. There were regions of both correlated bright and dark exciton emission, as well as regions with anticorrelated behavior: i.e., preferentially enhanced bright or preferentially

enhanced dark exciton emission (Figure S2). Related data for a different area of the same sample are shown in Figure S7.

Strongly correlated bright and dark exciton emission was most commonly observed. Anticorrelated behavior of variable degree was less common and was seen in some sample areas. As an example, there are two adjacent regions in the top right of the images in Figure 2a–d, one with intense dark exciton (marked by dotted circles) yet weak bright exciton emission, and vice versa (very top right corner).

We now analyze the relationship of bright and dark exciton emission with strain. Averaged cross sections of the highlighted regions in Figure 2c,d are shown in Figure 2e (top blue region) and Figure 2f (bottom red region), respectively. Strain (gray line), bright exciton intensity, and dark exciton intensity are shown for each cross section. Figure 2g,h shows the corresponding correlation plots for the data from Figure 2e,f, respectively. As can be seen, most of the heterogeneity in bright and dark exciton emission, when positively correlated, is associated with heterogeneity in strain. Conversely, for largely strain-free regions the emission varies little spatially. Also, despite some exceptions, when positively correlated, dark and bright exciton emission increases for both compressive and tensile strain: i.e., emission is generally weakest for low-strain regions with little topographic curvature.

Figure 3 shows the corresponding images of derived TEPL peak positions for bright  $X_0$  (Figure 3a) and dark  $X_D$  exciton (Figure 3b) emission. A spatiotemporal heterogeneity is observed with peak positions varying by  $\sim 0.02 \text{ eV}$  for both bright and dark excitons, suggesting a generally similar response to strain. Figure 3c,d shows the extracted dependence of peak position of  $X_0$  (Figure 3c) and  $X_D$  (Figure 3d) with strain for two selected areas indicated in Figure 3a,b. A continuous red shift is observed with decreasing compressive and increasing tensile strain, as expected and in agreement with previous observations for bright excitons.<sup>24,26,28,29</sup> However, as the two examples show, other than a common trend, the specific peak energy dependence in terms of absolute values and rate of change with strain varies spatially for the different sample regions (for additional data and analysis see Figures

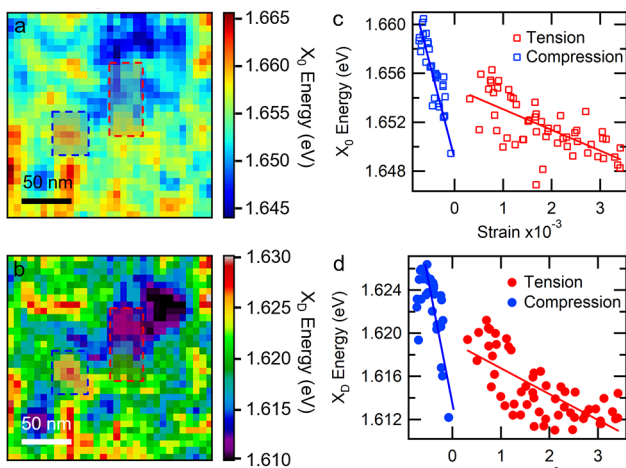


**Figure 3.** Images of TEPL spectral peak positions for the data from Figure 2 for (a) bright and (b) dark excitons. (c, d) Corresponding correlation graphs of peak positions for selected areas vs curvature-derived strain.

S4–S7). We attribute these differences to, for example, local variations in strain arising from other effects than sample curvature: e.g., substrate interaction induced during exfoliation, defects, or other structural heterogeneities.

We now performed approach curves at selected points of the sample with active strain modification through tip–sample force control. As is typical for cantilever AFM tips, below a critical distance the tip snaps into contact (Figure S1). Negative force values are tensile in nature and arise from tip–sample adhesion after the tip snaps into contact, while positive forces are compressive. Here we focused on the portion of the approach curve after snap-in, where the tip was in contact with the WSe<sub>2</sub> and actively applied a force by approaching or retracting the sample to and from the cantilever probe. A distance of 0 nm is defined as the distance at which the measured force changes from attractive to repulsive. As illustrated in Figure 4a, as representative regions we studied a topographically flat region (1), the top of a bubble (2), and its edge (3), with the corresponding bright and dark exciton PL intensity behavior shown in Figure 4b–d as a function of tip–sample force. The data were fit with a third-order polynomial as guide to the eye (solid curves).

On flat regions (Figure 4b), the dark exciton is weaker than the bright exciton emission, consistent with past observations,<sup>14</sup> and neither shows any discernible variation as a function of applied force. For reference, the data in Figure 2 were taken around +5 nN, i.e., a slightly compressive applied

force, which corresponds to 0 nm on the tip–sample distance scale in Figure 1d. In contrast, both the bright and dark exciton intensities evolved strongly with applied force on the bubble, as seen in Figure 4c. The initial rise in intensity with decreasing tensile force was due to Purcell enhancement with a decreasing mode volume with decreasing tip–substrate distance. It was followed by a downturn with increasing compressive force due to the onset of nonradiative quenching as the bubble was compressed and the WSe<sub>2</sub> to substrate distance shrank. This turnover happened at a larger applied force for the dark compared to the bright exciton. Note that the dark exciton intensity is on par with that of the bright exciton, as is consistently seen in areas of enhancement through this work. At the edge of the bubble (Figure 4d) a superposition behavior was observed, with weaker force dependence as expected, since the force-induced WSe<sub>2</sub> to substrate distance was less variable with applied force.

We first discuss the nanoscale spatial heterogeneity of the TEPL signal where both extrinsic and intrinsic effects contribute. Where associated with topography, a bubble in the WSe<sub>2</sub> monolayer and related elevation of the WSe<sub>2</sub> above the substrate modifies the picocavity mode volume and thus the degree of Purcell enhancement. However, bright and dark exciton emissions are affected differently, with their respective competition among near-field enhancement, Purcell effect, and quenching giving rise to their emission peaks at nominally different tip–sample distances by a few nanometers. This specifically explains why dark and bright excitons are enhanced to different degrees within the same area (for a ratio map between dark and bright intensities see Figure S2). We attribute this difference to the greater degree of localization experienced by the dark exciton: i.e., its spatially more confined emission. Both the bright and dark excitons quench as the picocavity formed by the tip–substrate interaction shrinks.<sup>14,29</sup> The bright exciton quenches before the dark exciton, which can explain the behavior seen for areas with strong dark exciton but reduced bright exciton emission. The slightly higher spatial resolution as seen for the dark vs bright exciton image in Figure 2 is also due to that higher degree of localization.

Several previous studies have analyzed how strain in a TMD monolayer affects its band structure, causing an associated bright exciton peak shift and emission intensity enhancement.<sup>21,22,24,26,28,29</sup> This work extends that observation to the dark exciton.

Note that the dark exciton is distinct from strain-localized excitons.<sup>24</sup> We also observe the lower-energy strain-localized exciton but only when strongly indenting the surface, while still seeing the dark exciton emission (Figure S3).

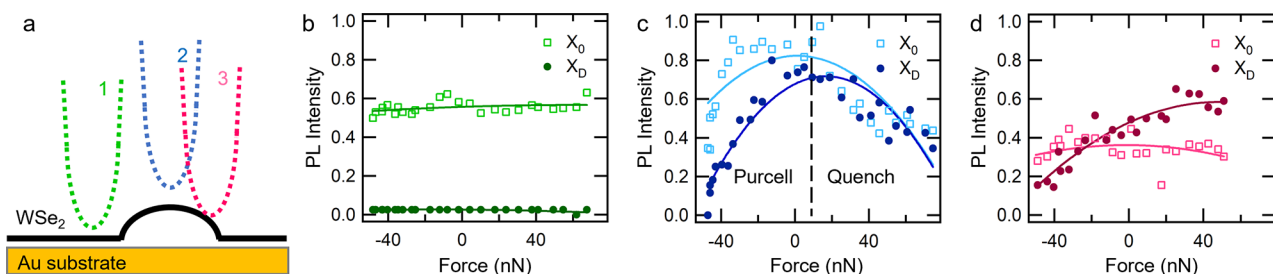


**Figure 4.** (a) Schematic of WSe<sub>2</sub> areas for correlated exciton force spectroscopy on flat (green), bubble (blue), and bubble edge (pink). Bright and dark exciton intensity as a function of applied tensile (negative values) and compressive (positive values) force on (b) the flat area, (c) the bubble top, and (d) the bubble edge.

Interestingly, the commonly observed intrinsic sample strain induced increase in emission intensity is correlated and linearly proportional for both bright and dark excitons, as seen by the near-parallel lines of best fit in Figure 2g. This suggests identical or at least similar mechanisms behind bright and dark exciton enhancement as related to the strain-induced modification of the band structure. This behavior is consistent with that of bright exciton funneling toward areas of greater tensile strain but counter to that of dark excitons funneling to areas of lesser strain.<sup>35–37</sup> However, previous funneling work was performed on dielectric surfaces. Our creation of a picocavity and the enhanced out-of-plane field from the tip–substrate geometry suggest that the Purcell enhancement may outcompete with funneling in this case. When the strain is negative (compressive), the PL intensity also increases as the magnitude of the strain increases, but at a faster rate (Figure 2h). At high exciton densities, there is a possibility of strain-dependent many-body recombinations.<sup>38,39</sup> We estimate a steady-state exciton density of approximately 1 electron per  $100 \times 100$  unit cells from a few picosecond lifetime, below the regime in which many-body recombinations play a significant role.

Both bright and dark excitons also respond similarly in terms of their spectral peak position with respect to strain (Figure 3). The observed blue shift for both excitons under compressive strain and red shift with increasing tensile strain is consistent with previous observations for bright excitons in WSe<sub>2</sub>, both supported and suspended.<sup>24,26,28,29</sup> The red shift of  $-20$  to  $-30$  meV per 0.1% strain aligns with previous measurements of  $-30$  to  $-95$  meV per 0.1% strain in TMDs.<sup>21,23,29</sup>

We note that while we refer to a single strain state in this discussion, the WSe<sub>2</sub> is actually in a mixed state at all times. When WSe<sub>2</sub> is bent, the top Se atoms move away from each other at the site of the bend, but the bottom Se atoms are forced closer to each other. This effect becomes less and less important as the bending radius increases, but with bending radii on the order of tens of nanometers, the spatial heterogeneity of strain and strain gradient are appreciable.

The combination of  $z$  scans and force spectroscopy both on flat regions and on bubbles provides a unique way to probe the interplay between strain and Purcell enhancement and their respective effect on bright and dark excitons. This active picocavity and strain tuning provides for a new degree of modification and control of exciton emission through the application of highly localized forces. In particular the force-controlled TEPL spectroscopy with the tip in contact with the bubble as enabled by dynamic and calibrated cantilever AFM probes has not been possible with conventional shear-force AFM-based TEPL.

As expected, no Purcell enhancement or quenching is seen after snap-in for approach curves in which the tip is on a flat area of WSe<sub>2</sub> (Figure 4a) and the signal remains constant. However, with the tip interacting with a bubble, an elastic deformation provides for simultaneous changes of both the picocavity mode volume and the degree of quenching depending on the WSe<sub>2</sub> to substrate distance. With increasing (positive) force quenching eventually dominates due to the reduced WSe<sub>2</sub>–substrate distance. Conversely, van der Waals force tip–WSe<sub>2</sub> pulling and an increase in the WSe<sub>2</sub> to substrate distance (negative force) will lead to a decrease in Purcell enhancement. A more complex behavior is seen at the edge of a bubble as a more heterogeneous superposition of both competing effects. Measurements performed on a suspended

TMD monolayer would not show this quenching behavior, as there is no metallic countersurface to form the picocavity.<sup>21,26</sup>

These active perturbation measurements show that the bright and dark excitons radiate at different rates once the tip is in contact with the material. The bright exciton intensity consistently peaks at approximately 0 nN of force, agreeing with past measurements that show the onset of quenching upon tip–sample contact.<sup>14,40,41</sup> In contrast, the dark exciton intensity peaks at higher values of applied force. The effect is most pronounced at the top of a bubble, likely due to the greater  $z$  position change that can occur under the same applied force and consistent with observations that the dark exciton is more sensitive to the local dielectric environment than the bright exciton.<sup>12,13</sup> The greater bending also causes a greater change in the strain state, as well as shrinks the mode volume of the picocavity. The bright exciton then quenches through dipole coupling, and energy transfer of the metal tip and substrate with the shrinking mode volume of the picocavity still allows for greater Purcell enhancement of the dark exciton emission before ultimately also being quenched.

In summary, we observe spatial variability of both bright and dark exciton emission in WSe<sub>2</sub>. The variations correlated with the strain in the material, with both compressive and tensile strain causing an increase in PL intensity. We see that greater tensile strain leads to an increase in peak intensity and a decrease in peak energy for both the bright and dark excitons, while compressive strain causes an increase in intensity and an increase in peak energy. Additionally, we can actively control the intensity of the TEPL through applied force from the AFM tip. Force applied on a bubble leads to an increase in peak intensity and then a decrease, while force applied to an area in which the WSe<sub>2</sub> is well-adhered shows no such change. The dark exciton reaches maximum intensity at a higher applied force than for the bright exciton due to the interplay between strain and Purcell enhancement. Through this work, we demonstrate the ability to use nano-localized strain to manipulate the excitonic behavior in WSe<sub>2</sub>, providing a route for potential active control of dark excitons in transition metal dichalcogenides.

## ■ ASSOCIATED CONTENT

### Data Availability Statement

The data generated in this study are available upon reasonable request.

### SI Supporting Information

The Supporting Information is available free of charge at <https://pubs.acs.org/doi/10.1021/acs.nanolett.2c03959>.

Force–distance dependence, bright and dark exciton emission ratios, strain-localized exciton, lateral distribution of bright and dark exciton energies, bright and dark exciton energy correlations, and additional data (PDF)

## ■ AUTHOR INFORMATION

### Corresponding Authors

Markus B. Raschke – Department of Physics and JILA, University of Colorado, Boulder, Colorado 80309, United States;  [orcid.org/0000-0003-2822-851X](https://orcid.org/0000-0003-2822-851X); Email: [markus.raschke@colorado.edu](mailto:markus.raschke@colorado.edu)

Kyoung-Duck Park – Department of Physics, Pohang University of Science and Technology (POSTECH), Pohang 37673, Republic of Korea;  [orcid.org/0000-0002-9302-9384](https://orcid.org/0000-0002-9302-9384); Email: [parklab@postech.ac.kr](mailto:parklab@postech.ac.kr)

## Authors

Kathryn Hasz – Department of Physics and JILA, University of Colorado, Boulder, Colorado 80309, United States; Department of Physics, Carthage College, Kenosha, Wisconsin 53140, United States;  orcid.org/0000-0003-3089-2882

Zuocheng Hu – Department of Physics and JILA, University of Colorado, Boulder, Colorado 80309, United States

Complete contact information is available at:  
<https://pubs.acs.org/10.1021/acs.nanolett.2c03959>

## Author Contributions

K.H., K.-D.P., and M.B.R. conceived the research. K.H. and Z.H. performed the experiments. K.H., Z.H., and M.B.R. analyzed the data. K.H. and M.B.R. discussed and wrote the manuscript. All the authors read and provided comments on the manuscript.

## Notes

The authors declare no competing financial interest.

## ACKNOWLEDGMENTS

The work was supported by the U.S. Department of Energy, Office of Basic Energy Sciences, under Award No. DE-SC0008807. K.-D.P. was supported by the MSIT, Korea, under the ITRC support program (IITP-2022-RS-2022-00164799) supervised by the IITP. We are indebted to Andrey Krayev and Horiba Instruments Inc. for technical support. We thank Fabian Menges, Ben Whetten, and Wenjin Luo for valuable discussions.

## REFERENCES

- (1) Zhao, W.; Ghorannevis, Z.; Chu, L.; Toh, M.; Kloc, C.; Tan, P.-H.; Eda, G. Evolution of electronic structure in atomically thin sheets of WS<sub>2</sub> and WSe<sub>2</sub>. *ACS Nano* **2013**, *7*, 791–797.
- (2) Zhang, X. X.; You, Y.; Zhao, S. Y. F.; Heinz, T. F. Experimental Evidence for Dark Excitons in Monolayer WSe<sub>2</sub>. *Phys. Rev. Lett.* **2015**, *115*, 1–6.
- (3) He, K.; Kumar, N.; Zhao, L.; Wang, Z.; Mak, K. F.; Zhao, H.; Shan, J. Tightly Bound Excitons in Monolayer WSe<sub>2</sub>. *Phys. Rev. Lett.* **2014**, *113*, 026803.
- (4) Chernikov, A.; Berkelbach, T. C.; Hill, H. M.; Rigosi, A.; Li, Y.; Aslan, O. B.; Reichman, D. R.; Hybertsen, M. S.; Heinz, T. F. Exciton Binding Energy and Nonhydrogenic Rydberg Series in Monolayer WS<sub>2</sub>. *Phys. Rev. Lett.* **2014**, *113*, 076802.
- (5) Ugeda, M. M.; Bradley, A. J.; Shi, S.-f.; Jornada, F. H.; Zhang, Y.; Qiu, D. Y.; Ruan, W.; Mo, S.-k.; Hussain, Z.; Shen, Z.-x.; Wang, F.; Louie, S. G.; Crommie, M. F. Giant bandgap renormalization and excitonic effects in a monolayer transition metal dichalcogenide semiconductor. *Nat. Mater.* **2014**, *13*, 1091–1095.
- (6) Mak, K. F.; Shan, J. Photonics and optoelectronics of 2D semiconductor transition metal dichalcogenides. *Nature Publishing Group* **2016**, *10*, 216–226.
- (7) Baugher, B. W. H.; Churchill, H. O. H.; Yang, Y.; Jarillo-herrero, P. Optoelectronic devices based on electrically tunable p – n diodes in a monolayer dichalcogenide. *Nat. Nanotechnol.* **2014**, *9*, 262–267.
- (8) Shanks, D. N.; Mahdikhanyarservejahany, F.; Muccianti, C.; Alfrey, A.; Koehler, M. R.; Mandrus, D. G.; Taniguchi, T.; Watanabe, K.; Yu, H.; LeRoy, B. J.; Schaibley, J. R. Nanoscale trapping of interlayer excitons in a 2D semiconductor heterostructure. *Nano Lett.* **2021**, *21*, 5641–5647.
- (9) Malic, E.; Selig, M.; Feierabend, M.; Brem, S.; Christiansen, D.; Wendler, F.; Knorr, A.; Berghäuser, G. Dark excitons in transition metal dichalcogenides. *Physical Review Materials* **2018**, *2*, 1–7.
- (10) Zhang, X. X.; Cao, T.; Lu, Z.; Lin, Y. C.; Zhang, F.; Wang, Y.; Li, Z.; Hone, J. C.; Robinson, J. A.; Smirnov, D.; Louie, S. G.; Heinz, T. F. Magnetic brightening and control of dark excitons in monolayer WSe<sub>2</sub>. *Nat. Nanotechnol.* **2017**, *12*, 883–888.
- (11) Zhou, Y.; Scuri, G.; Wild, D. S.; High, A. A.; Dibos, A.; Jauregui, L. A.; Shu, C.; Greve, K. D.; Pistunova, K.; Joe, A. Y.; Taniguchi, T.; Watanabe, K.; Kim, P.; Lukin, M. D.; Park, H. Probing dark excitons in atomically thin semiconductors via near-field coupling to surface plasmon polaritons. *Nat. Nanotechnol.* **2017**, *12*, 856–860.
- (12) Ao, X.; Xu, X.; Dong, J.; He, S. Unidirectional Enhanced Emission from 2D Monolayer Suspended by Dielectric Pillar Array. *ACS Appl. Mater. Interfaces* **2018**, *10*, 34817–34821.
- (13) Lo, T. W.; Chen, X.; Zhang, Z.; Zhang, Q.; Leung, C. W.; Zayats, A. V.; Lei, D. Plasmonic Nanocavity Induced Coupling and Boost of Dark Excitons in Monolayer WSe<sub>2</sub> at Room Temperature. *Nano Lett.* **2022**, *22*, 1915–1921.
- (14) Park, K. D.; Jiang, T.; Clark, G.; Xu, X.; Raschke, M. B. Radiative control of dark excitons at room temperature by nano-optical antenna-tip Purcell effect. *Nat. Nanotechnol.* **2018**, *13*, 59–64.
- (15) Robert, C.; Amand, T.; Cadiz, F.; Lagarde, D.; Courtade, E.; Manca, M.; Taniguchi, T.; Watanabe, K.; Urbaszek, B.; Marie, X. Fine structure and lifetime of dark excitons in transition metal dichalcogenide monolayers. *Phys. Rev. B* **2017**, *96*, 1–8.
- (16) Li, Z.; Wang, T.; Jin, C.; Lu, Z.; Lian, Z.; Meng, Y.; Blei, M.; Gao, S.; Taniguchi, T.; Watanabe, K.; et al. Emerging photoluminescence from the dark-exciton phonon replica in monolayer WSe<sub>2</sub>. *Nat. Commun.* **2019**, *10*, 1–7.
- (17) Smoleński, T.; Kazimierczuk, T.; Goryca, M.; Wojnar, P.; Kossacki, P. Mechanism and dynamics of biexciton formation from a long-lived dark exciton in a CdTe quantum dot. *Phys. Rev. B* **2015**, *91*, 155430.
- (18) Combescot, M.; Betbeder-Matibet, O.; Combescot, R. Bose-Einstein condensation in semiconductors: The key role of dark excitons. *Phys. Rev. Lett.* **2007**, *99*, 176403.
- (19) Poem, E.; Kodriano, Y.; Tradonsky, C.; Lindner, N.; Gerardot, B.; Petroff, P.; Gershoni, D. Accessing the dark exciton with light. *Nat. Phys.* **2010**, *6*, 993–997.
- (20) Vasconcelos, R.; Bragança, H.; Qu, F.; Fu, J. Dark exciton brightening and its engaged valley dynamics in monolayer WSe<sub>2</sub>. *Phys. Rev. B* **2018**, *98*, 195302.
- (21) Aslan, B.; Yule, C.; Yu, Y.; Lee, Y. J.; Heinz, T. F.; Cao, L.; Brongersma, M. L. Excitons in strained and suspended monolayer WSe<sub>2</sub>. *2D Materials* **2022**, *9*, 015002.
- (22) Blundo, E.; Felici, M.; Yildirim, T.; Pettinari, G.; Tedeschi, D.; Miriametro, A.; Liu, B.; Ma, W.; Lu, Y.; Polimeni, A. Evidence of the direct-to-indirect band gap transition in strained two-dimensional WS<sub>2</sub>, MoS<sub>2</sub>, and WSe<sub>2</sub>. *Physical Review Research* **2020**, *2*, 1–7.
- (23) Cianci, S.; Blundo, E.; Felici, M.; Polimeni, A.; Pettinari, G. Tailoring the optical properties of 2D transition metal dichalcogenides by strain. *Opt. Mater.* **2022**, *125*, 112087.
- (24) Darlington, T. P.; Carmesin, C.; Florian, M.; Yanev, E.; Ajayi, O.; Ardelean, J.; Rhodes, D. A.; Ghiotto, A.; Krayev, A.; Watanabe, K.; et al. Imaging strain-localized excitons in nanoscale bubbles of monolayer WSe<sub>2</sub> at room temperature. *Nat. Nanotechnol.* **2020**, *15*, 854–860.
- (25) Mondal, N.; Azam, N.; Gartstein, Y. N.; Mahjour-Samani, M.; Malko, A. V. Photoexcitation Dynamics and Long-Lived Excitons in Strain-Engineered Transition Metal Dichalcogenides. *Adv. Mater.* **2022**, *34*, 2110568.
- (26) Gelly, R. J.; Renaud, D.; Liao, X.; Pingault, B.; Bogdanovic, S.; Scuri, G.; Watanabe, K.; Taniguchi, T.; Urbaszek, B.; Park, H.; Lončar, M. Probing dark exciton navigation through a local strain landscape in a WSe<sub>2</sub> monolayer. *Nat. Commun.* **2022**, *13*, 1–7.
- (27) Lee, J.; Yun, S. J.; Seo, C.; Cho, K.; Kim, T. S.; An, G. H.; Kang, K.; Lee, H. S.; Kim, J. Switchable, tunable, and directable exciton funneling in periodically wrinkled WS<sub>2</sub>. *Nano Lett.* **2021**, *21*, 43–50.
- (28) Oliva, R.; Wozniak, T.; Faria, P. E.; Dybala, F.; Kopaczek, J.; Fabian, J.; Scharoch, P.; Kudrawiec, R. Strong Substrate Strain Effects in Multilayered WS<sub>2</sub> Revealed by High-Pressure Optical Measurements. *ACS Appl. Mater. Interfaces* **2022**, *14*, 19857–19868.

- (29) Park, K. D.; Khatib, O.; Kravtsov, V.; Clark, G.; Xu, X.; Raschke, M. B. Hybrid Tip-Enhanced Nanospectroscopy and Nanoimaging of Monolayer WSe<sub>2</sub> with Local Strain Control. *Nano Lett.* **2016**, *16*, 2621–2627.
- (30) Sader, J. E.; Larson, I.; Mulvaney, P.; White, L. R. Method for the calibration of atomic force microscope cantilevers. *Rev. Sci. Instrum.* **1995**, *66*, 3789–3798.
- (31) Darlington, T. P.; Krayev, A.; Venkatesh, V.; Saxena, R.; Kysar, J. W.; Borys, N. J.; Jariwala, D.; Schuck, P. J. Facile and quantitative estimation of strain in nanobubbles with arbitrary symmetry in 2D semiconductors verified using hyperspectral nano-optical imaging. *J. Chem. Phys.* **2020**, *153*, 024702.
- (32) Khestanova, E.; Guinea, F.; Fumagalli, L.; Geim, A. K.; Grigorieva, I. V. Universal shape and pressure inside bubbles appearing in van der Waals heterostructures. *Nat. Commun.* **2016**, *7*, 1–10.
- (33) Dieter, G. E.; Bacon, D. *Mechanical metallurgy*; McGraw-Hill: 1976; Vol. 3, pp 43–53.
- (34) Landau, L. D.; Lifšic, E. M.; Lifshitz, E. M.; Kosevich, A. M.; Pitaevskii, L. P. *Theory of elasticity*; Butterworth-Heinemann: 1986; Vol. 7, pp 44–68.
- (35) Su, H.; Xu, D.; Cheng, S.-W.; Li, B.; Liu, S.; Watanabe, K.; Taniguchi, T.; Berkelbach, T. C.; Hone, J. C.; Delor, M. Dark-exciton driven energy funneling into dielectric inhomogeneities in two-dimensional semiconductors. *Nano Lett.* **2022**, *22*, 2843–2850.
- (36) Rosati, R.; Schmidt, R.; Brem, S.; Perea-Causin, R.; Niehues, I.; Kern, J.; Preuß, J. A.; Schneider, R.; Michaelis de Vasconcellos, S.; Bratschitsch, R.; et al. Dark exciton anti-funneling in atomically thin semiconductors. *Nat. Commun.* **2021**, *12*, 1–7.
- (37) Castellanos-Gomez, A.; Roldán, R.; Cappelluti, E.; Buscema, M.; Guinea, F.; van der Zant, H. S.; Steele, G. A. Local strain engineering in atomically thin MoS<sub>2</sub>. *Nano Lett.* **2013**, *13*, 5361–5366.
- (38) Danovich, M.; Zólyomi, V.; Fal'ko, V. I.; Aleiner, I. L. Auger recombination of dark excitons in WS<sub>2</sub> and WSe<sub>2</sub> monolayers. *2D Materials* **2016**, *3*, 035011.
- (39) Kim, H.; Uddin, S. Z.; Higashitrumizu, N.; Rabani, E.; Javey, A. Inhibited nonradiative decay at all exciton densities in monolayer semiconductors. *Science* **2021**, *373*, 448–452.
- (40) May, M. A.; Jiang, T.; Du, C.; Park, K. D.; Xu, X.; Belyanin, A.; Raschke, M. B. Nanocavity Clock Spectroscopy: Resolving Competing Exciton Dynamics in WSe<sub>2</sub>/MoSe<sub>2</sub> Heterobilayers. *Nano Lett.* **2021**, *21*, 522–528.
- (41) Kravtsov, V.; Berweger, S.; Atkin, J. M.; Raschke, M. B. Control of Plasmon Emission and Dynamics at the Transition from Classical to Quantum Coupling. *Nano Lett.* **2014**, *14*, 5270–5275–.

## □ Recommended by ACS

### Real-Time Diagnostics of 2D Crystal Transformations by Pulsed Laser Deposition: Controlled Synthesis of Janus WSSe Monolayers and Alloys

Sumner B. Harris, David B. Geohegan, et al.

JANUARY 17, 2023

ACS NANO

READ ▶

### Moiré Potential, Lattice Relaxation, and Layer Polarization in Marginally Twisted MoS<sub>2</sub> Bilayers

Nikhil Tilak, Eva Y. Andrei, et al.

DECEMBER 28, 2022

NANO LETTERS

READ ▶

### Enhancing the Purity of Deterministically Placed Quantum Emitters in Monolayer WSe<sub>2</sub>

Christopher E. Stevens, Joshua R. Hendrickson, et al.

NOVEMBER 29, 2022

ACS NANO

READ ▶

### Stability of the In-Plane Room Temperature van der Waals Ferromagnet Chromium Ditelluride and Its Conversion to Chromium-Interleaved CrTe<sub>2</sub> Compounds

Anike Purbawati, Johann Coraux, et al.

JANUARY 18, 2023

ACS APPLIED ELECTRONIC MATERIALS

READ ▶

Get More Suggestions >